

**Imaging nitrogen fixation at lithium solid electrolyte interphases via cryo-electron  
microscopy**

Katherine Steinberg<sup>1</sup>, Xintong Yuan<sup>2</sup>, Nikifar Lazouski<sup>1</sup>, Channing K. Klein<sup>3</sup>,  
Karthish Manthiram<sup>3\*</sup>, and Yuzhang Li<sup>2\*</sup>

<sup>1</sup>Department of Chemical Engineering, Massachusetts Institute of Technology, Cambridge, MA  
02139, USA

<sup>2</sup>Department of Chemical & Biomolecular Engineering, University of California, Los Angeles,  
Los Angeles, CA 90095, USA

<sup>3</sup>Division of Chemistry and Chemical Engineering, California Institute of Technology, Pasadena,  
CA 91125, USA

\*Correspondence: [yuzhangli@ucla.edu](mailto:yuzhangli@ucla.edu), [karthish@caltech.edu](mailto:karthish@caltech.edu)

## Abstract

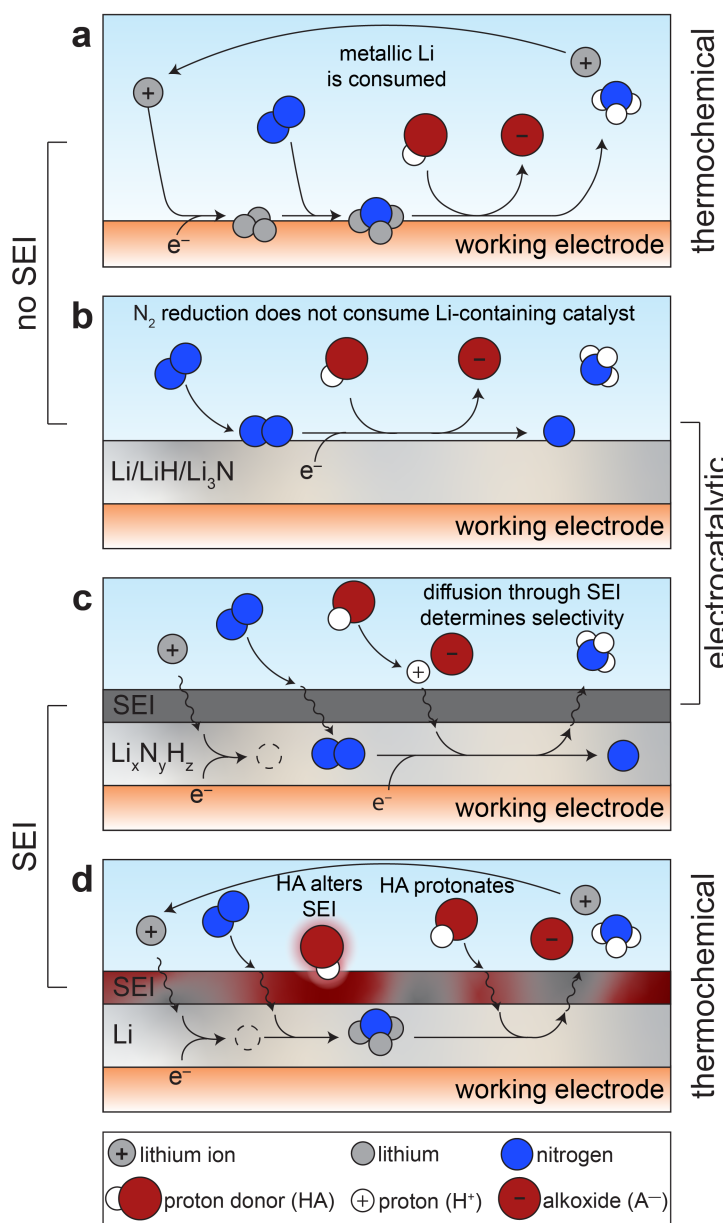
Electrifying ammonia synthesis will be vital to the decarbonization of the chemical industry, as the Haber-Bosch process contributes significantly to global carbon emissions. A lithium-mediated pathway is among the most promising ambient-condition electrochemical ammonia synthesis methods. However, the role of metallic lithium and its passivation layer, the solid electrolyte interphase (SEI), remains unresolved. Here, we apply a multiscale approach that leverages the powerful cryogenic transmission electron microscopy (cryo-TEM) technique to reveal new insights that were previously inaccessible with conventional methods. We discover that the proton donor (e.g. ethanol) governs lithium reactivity toward nitrogen fixation. Without ethanol, the SEI passivates lithium metal, rendering it inactive for ammonia production. Ethanol disrupts this passivation layer, enabling continuous reactivity at the lithium surface. As a result, metallic lithium is consumed via reactions with nitrogen, proton donor, and other electrolyte components. This reactivity across the SEI is vital to device-level performance of lithium-mediated ammonia synthesis.

**Keywords:** Electrochemistry, ammonia synthesis, lithium-mediated, solid electrolyte interphase, cryo-electron microscopy, chemical corrosion, nitrogen fixation

With an annual production of over 180 million tons,<sup>1</sup> ammonia ( $\text{NH}_3$ ) is among the most important commodity chemicals. While ~80% of ammonia is used in producing fertilizers,<sup>1,2</sup> it is also the main source of nitrogen functionality in chemical synthesis<sup>3</sup> and may be a key energy carrier as industry decarbonizes.<sup>4,5</sup> The predominant method of ammonia generation is the Haber-Bosch process, which demands high temperatures (400-500°C) and pressures (150-250 bar) to react nitrogen and hydrogen, usually using hydrogen from steam-methane reforming.<sup>5,6</sup> As a result, each ton of ammonia produced generates upwards of 1.9 tons of  $\text{CO}_2$ , contributing 1-2% of global carbon emissions.<sup>7,8</sup> Due to the complexity of the Haber-Bosch process, it is only economical at large scales, leading to centralized production that creates disparities in access to fertilizer.<sup>7,9</sup> These limitations motivate the development of electrochemical ammonia synthesis methods, which could be modular, easily-integrated with intermittent renewable electricity, and utilize water electrolysis, eliminating the need for hydrocarbon-derived hydrogen.<sup>8,10</sup>

One of the most promising ambient-condition electrochemical methods for ammonia synthesis is the lithium-mediated pathway. This process takes advantage of the facile and thermodynamically-favorable reaction between dinitrogen and metallic lithium,<sup>11</sup> generating ammonia by electrodepositing lithium from an organic electrolyte, often  $\text{LiBF}_4$  or  $\text{LiClO}_4$  in tetrahydrofuran (THF), that contains nitrogen and a proton donor.<sup>12-15</sup> Lithium-mediated electrochemical ammonia synthesis (LiMEAS) has been rigorously vetted by control experiments<sup>14-16</sup> and achieves the highest rates and Faradaic efficiencies (FEs) to date among ambient-temperature electrochemical ammonia synthesis processes.<sup>17-19</sup> The efficiency of LiMEAS has improved significantly from its first reported implementations in 1930<sup>20</sup> and 1993<sup>12</sup> with developments such as the use of gas diffusion electrodes,<sup>17</sup> pulsed currents,<sup>21</sup> a phosphonium salt proton shuttle,<sup>18</sup> and the addition of low concentrations of oxygen.<sup>19</sup>

However, the role of lithium in LiMEAS is still under debate. Some studies propose that electrochemically-deposited lithium is consumed by thermochemical nitridation and protonation steps to generate ammonia and lithium ethoxide – a pathway classified as thermochemical because the nitrogen fixation step is thermochemical (Fig. 1a).<sup>12–14,22</sup> Other works propose an electrocatalytic mechanism, in which a layer of lithium, lithium nitride, or lithium hydride adsorbs, protonates, and reduces nitrogen to make ammonia without directly being consumed, thereby acting as an electrocatalyst (Fig. 1b).<sup>21,23</sup>



A primary source of complexity in LiMEAS is the solid electrolyte interphase (SEI), a passivation film that forms spontaneously in all electrochemical lithium cells.<sup>24,25</sup> The SEI consists of both organic and inorganic electrolyte breakdown products and can vary in composition and structure depending on electrolyte chemistry and operating

**Fig. 1 | Schematic of proposed reaction mechanisms of lithium-mediated ammonia synthesis. a,** Thermochemical mechanism proposed in Ref. 14. **b,** Electrocatalytic mechanism proposed in Ref. 23. **c,** SEI transport model proposed in Ref. 21. **d,** SEI permeability model proposed in Ref. 29.

conditions.<sup>26,27</sup> The SEI is assumed to be electronically insulating and ionically conductive; its local properties dictate transport of lithium ions at the electrode-electrolyte interface and thus the morphology of lithium deposits.<sup>28</sup>

The SEI is often invoked to explain observed phenomena in LiMEAS, yet our understanding of its role is still incomplete. One study proposes that relative transport rates of lithium ions, nitrogen, and protons through a nonreactive SEI are the most influential factor in determining selectivity, with imbalance in diffusion rates leading to undesirable buildup of metallic lithium or lithium nitride, or excessive hydrogen evolution (Fig. 1c).<sup>21</sup> Our group has also emphasized the importance of transport through the SEI, proposing that proton donor identity and concentration impact whether the SEI is permeable to nitrogen diffusion (Fig. 1d).<sup>29</sup> Other works have taken steps to directly detect surface species in LiMEAS, using lithium stripping,<sup>22,23,30</sup> titration measurements of lithium nitride,<sup>14,23,30</sup> and X-ray characterization techniques<sup>19,30</sup> to probe surface chemistry. While these studies provide insights into the composition of the lithium surface, none yet have resolved the debate over the molecular-scale mechanism of LiMEAS because lithium metal and its SEI cannot be characterized with sufficient spatial resolution using conventional techniques.

Here we have taken a multiscale approach to understanding of the role of surface chemistry in LiMEAS. We combined bulk quantification of key products, scanning electron microscopy (SEM), and X-ray photoelectron spectroscopy (XPS) with cryo-transmission electron microscopy (cryo-TEM), leveraging the nanoscopic resolution that has given this technique such utility in the battery field.<sup>27,28,31,32</sup> Our results reveal that surface chemistry in LiMEAS is quite distinct from that present in lithium batteries. We observed that lithium nitridation is highly sensitive to surface passivation; in the absence of a proton donor (e.g.

ethanol), the SEI inhibits reactivity between lithium and nitrogen. We found that the addition of ethanol disrupts the formation of a passivating SEI, enabling continuous surface reactivity that consumes metallic lithium as it deposits. Contrary to lithium batteries that require SEI passivation for reversible energy storage, we show that LiMEAS operates via continuous thermochemical consumption of poorly-passivated lithium.

### **Model systems for systematic study of surface reactivity**

Most of what is known about the SEI is from research on lithium batteries, which generally use aprotic organic solvents and inert argon atmospheres. In contrast, LiMEAS has two added sources of reactivity: a proton donor and nitrogen gas. We set out to understand how these components change the surface chemistry of lithium by varying the presence of each species in four model systems:

- A) Ar gas, no proton donor (“no HA”)
- B) N<sub>2</sub> gas, no proton donor (“no HA”)
- C) Ar gas, 0.1 M EtOH
- D) N<sub>2</sub> gas, 0.1 M EtOH

It is important to note that the conditions used – ambient pressure, ethanol as proton donor, low current density, and flooded electrodes – were chosen for ease of characterization, not for optimal performance (Fig. 2a, Supplementary Discussion).

### **Quantification of Key Products**

To better understand reactivity at the lithium surface in LiMEAS, the major reaction products were quantified for each of the four model systems, revealing that the presence or absence of proton donor is the most important factor in determining the partitioning of FE.

Ammonia can be measured using the salicylate assay,<sup>14,33</sup> while lithium nitride or other fixed nitrogen species ( $\text{Li}_x\text{N}_y\text{H}_z$ ) can be quantified via acid titration followed by the salicylate assay, keeping in mind potential limitations with detecting small amounts of ammonia (see Supplementary Discussion). Unsurprisingly, only system D, which contains both nitrogen and ethanol, generates ammonia (Fig. 2c). Intriguingly, we found that lithium nitride is only detected when both nitrogen and ethanol are present, whereas lithium and nitrogen appear not to react in the absence of proton donor (system B) (Fig. 2d). This suggests that dinitrogen cannot permeate

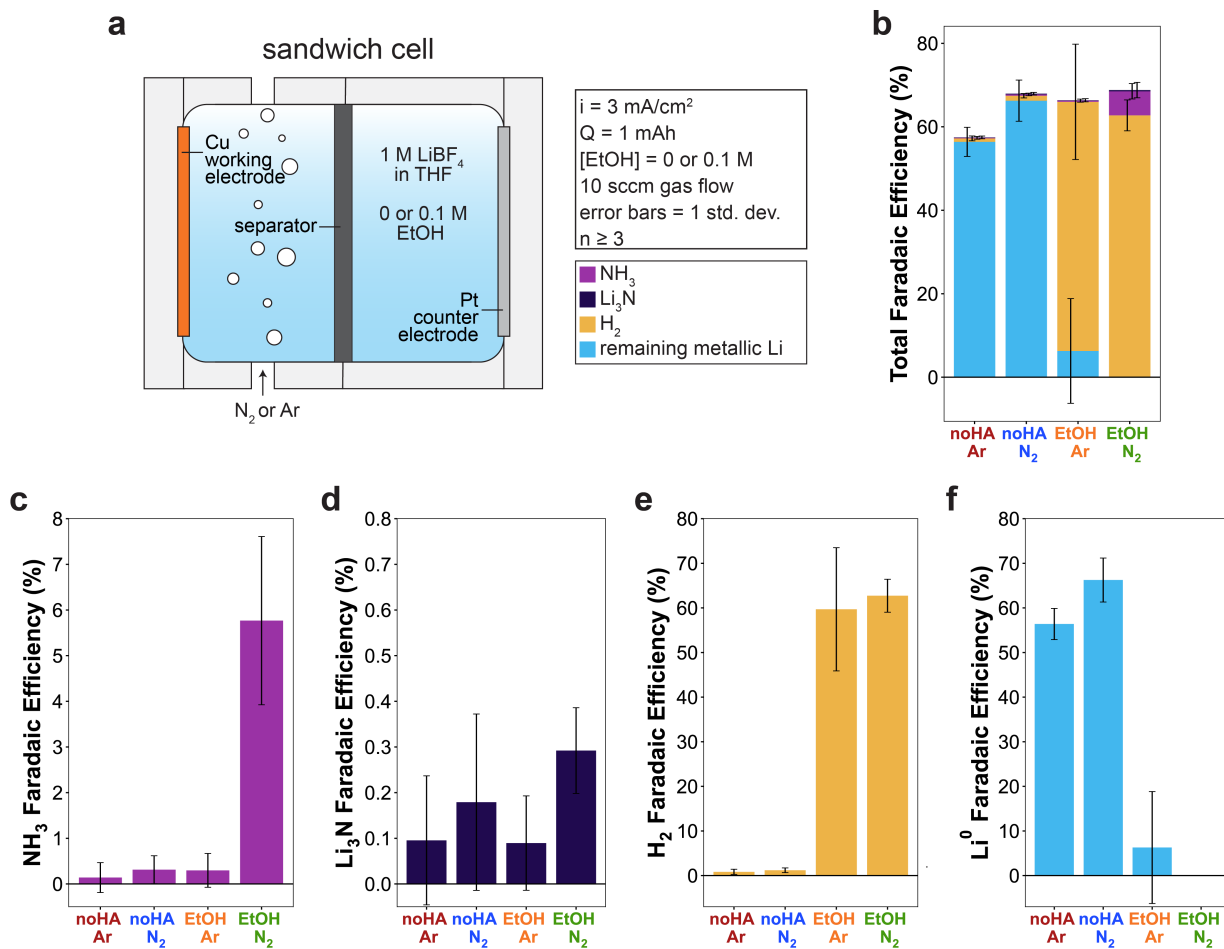


**Fig. 2 | Quantification of key products.** **a**, Diagram of cell setup and conditions used in these experiments. **b**, Total Faradaic efficiencies of quantified products. Error bars are staggered such that they represent  $\text{Li}^0$ ,  $\text{H}_2$ ,  $\text{NH}_3$ , and  $\text{Li}_3\text{N}$  from left to right. **c**, Average ammonia Faradaic efficiencies. **d**, Average lithium nitride Faradaic efficiencies. **e**, Average dihydrogen Faradaic efficiencies. **f**, Average electrochemically-connected remaining metallic lithium Faradaic efficiencies. Error bars for all plots are one standard deviation,  $n \geq 3$ . Raw data are included in Supplementary Tables.

the native SEI film. In agreement with prior measurements,<sup>14,23,30</sup> the detected Li<sub>3</sub>N in system D is present in very small quantities – about 0.3% FE. This result supports the hypothesis that the protonation step in LiMEAS is fast, and fixed nitrogen species are short-lived on the electrode surface.<sup>14,30</sup>

Another important side product in LiMEAS is hydrogen gas, which can be quantified via on-line gas chromatography (GC) measurements (Fig. 2e). The hydrogen FE increases from <2% in the absence of proton donor to ~60% with the addition of ethanol, indicating that the majority of generated hydrogen originates from ethanol. Because only 1 mAh of charge is passed in total, the H<sub>2</sub> FEs with proton donor reflect only ~6-7% consumption of the ethanol in the electrolyte (Supplementary Fig. 4a). The average H<sub>2</sub> FE with proton donor appears independent of feed gas, though the argon case has greater variability. Hydrogen measured in the absence of proton donor may be the result of trace water reduction or THF decomposition at the lithium surface.

By galvanostatically stripping the electrode after experiments, we can obtain an estimate of the electrochemically-connected metallic lithium remaining on the surface (Fig. 2f).<sup>34,35</sup> Once again, the strongest predictor of yield in this measurement is the presence or absence of proton donor, with the systems lacking proton donor accumulating strippable lithium corresponding to more than half the charge passed. In the cases with ethanol added, all but one of the replicates we performed had zero electrochemically-connected lithium (Supplementary Fig. 6-7). Overall, it appears that when ethanol is present in solution, metallic lithium is largely consumed through reactions with ethanol, nitrogen, and other electrolyte components.

Summing the FEs of quantified products accounts for 60-70% of the total charge passed (Fig. 2b). This is reasonable for lithium electroplating, as the remaining charge likely goes to

“inactive” or non-electrochemically-connected lithium and SEI-forming reactions (See Supplementary Discussion).<sup>35</sup>

### **Imaging the Lithium Surface**

Our product quantification results indicate stark differences in reactivity with and without proton donor, even for reactions that do not directly involve ethanol. To understand this phenomenon, we reveal surface morphology of the four model systems using SEM. For the two cases without proton donor, the lithium deposit is essentially identical in morphology, with a mix of lithium filaments and larger agglomerations commonly observed in lithium metal batteries (Fig. 3a,b).<sup>28,31</sup> With the addition of proton donor, the morphology changes significantly; instead of a dense layer of lithium filaments, there are round deposits that leave the underlying Cu foils exposed in several places (Fig. 3c,d). Particle size varies with the feed gas: particles plated under an argon atmosphere range in size up to ~2-3  $\mu\text{m}$ , while those obtained under a nitrogen atmosphere are ~0.8-0.9  $\mu\text{m}$  in diameter (Supplementary Fig. 13). Blurriness from electron-beam induced charging indicates that these particles are electrically insulating, suggesting a strong presence of SEI rather than metallic lithium.

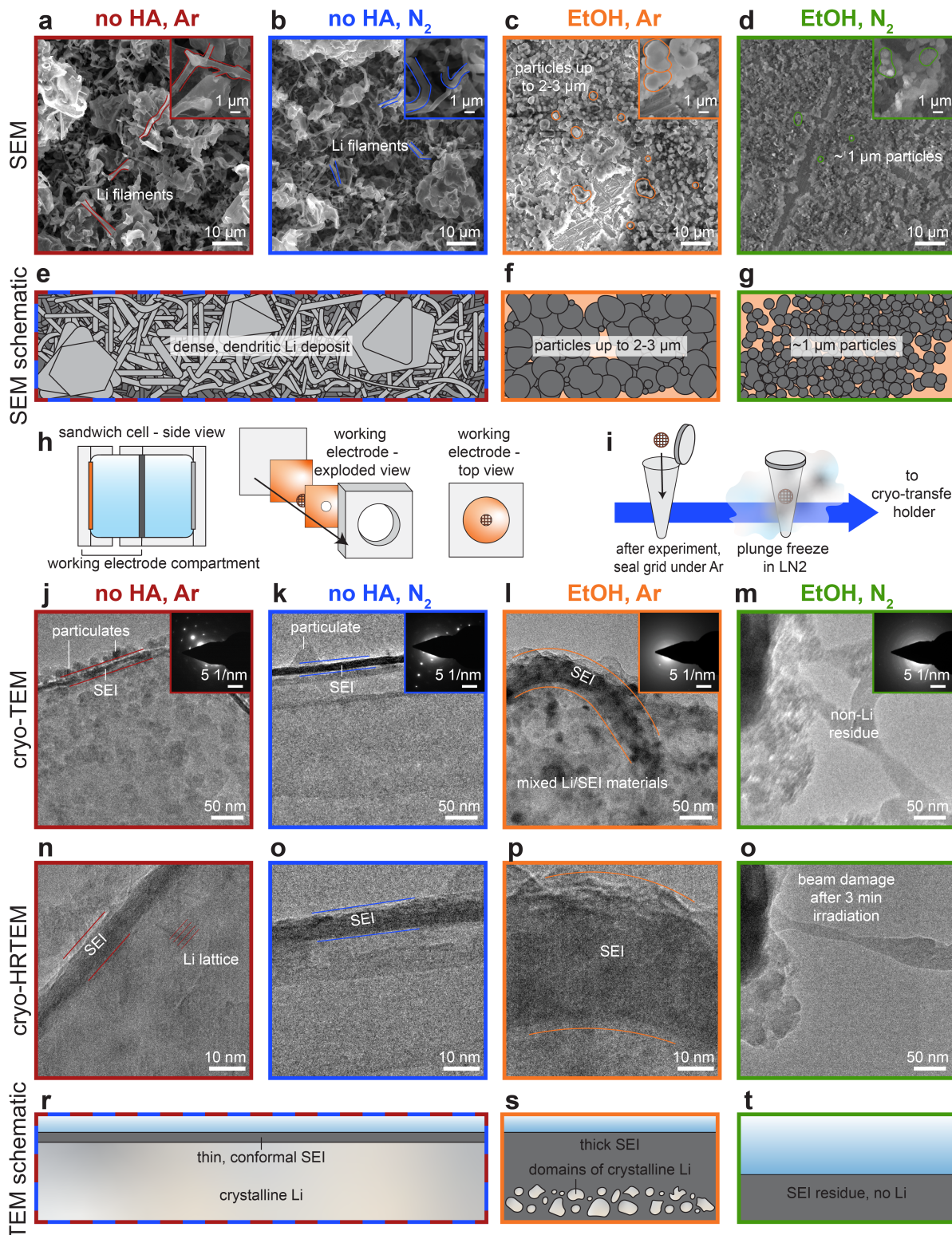


**Fig. 3 | Imaging results from the four model systems.** **a-d**, SEM images, with insets at higher magnification. **e-g**, Illustration of observed morphology at SEM scale. **h**, Illustration of cell setup for cryo-EM experiments. **i**, Illustration of cryo-EM sample preparation process. **j-m**, Cryo-TEM images, with inset SAED images. **n-p**, High-resolution cryo-TEM images. **q**, Beam damage observed in EtOH/N<sub>2</sub> case. **r-t**, Illustration of SEI observations via cryo-TEM. Enlarged versions of images are available in Supplementary Figures 6-14.

The absence of metallic lithium deposits in systems with ethanol imply that there could be differences in surface passivation with the addition of proton donor. Cryo-TEM can preserve these reactive surface structures, allowing us to understand the role of SEI in promoting these morphologies. Metallic lithium and its SEI are highly beam-sensitive in conventional TEM, but cryogenic temperatures stabilize and preserve their native state, enabling high-resolution observation of the SEI.<sup>31</sup> To leverage cryo-TEM, we placed TEM grids at the working electrode of each cell (Fig. 3h), then after the experiment, the grids were plunge-frozen in liquid nitrogen (Fig. 3i). Consistent with prior literature, we saw no evidence of reactivity between metallic lithium and liquid nitrogen in EDS mapping of cryo-EM samples (Supplementary Fig. 19-22).<sup>31</sup>

Cryo-TEM reveals that the interfacial morphology of samples without proton donor (systems A and B) resembles other lithium deposits documented in the cryo-EM battery literature.<sup>28,31</sup> Selected area electron diffraction (SAED) patterns reveal crystalline lithium viewed along the [111] zone axis, and in certain high-resolution (HR) images, it is possible to distinguish atoms arranged in a crystalline lattice (Fig. 3j-k,n-o; Supplementary Fig. 18a-b). The SEI is observed as a darker-contrast region at the surface of the lithium. It appears amorphous in structure and is approximately 7-9 nm thick for both of the samples that lack proton donor, regardless of whether argon or nitrogen was the feed gas. In some areas, this conformal SEI has other particulates on top of it, indicating some kind of loosely-bound extended SEI may exist.<sup>36</sup>

In the system with ethanol and argon (system C), the SEI morphology changes significantly (Fig 3l,p). SAED shows evidence of crystalline lithium but an incomplete diffraction pattern (Supplementary Fig. 18c). The SEI is thicker (40-60 nm) and more disordered, and it blankets domains of crystalline lithium that are mixed with SEI-type materials. The system with both ethanol and nitrogen (system D) diverges even further from typical lithium

morphology (Fig 3m,q). Little material remains on the TEM grid, and what does persist is very beam-sensitive, preventing HRTEM imaging. SAED confirms that the material left on the surface is amorphous (Supplementary Fig. 18d). These observations imply that this is SEI-type material and not metallic lithium.

### Revealing mechanisms of SEI disruption

Our cryo-TEM results clearly demonstrate that adding ethanol disrupts the formation of a passivating SEI, leading to a disordered interfacial morphology quite different from the conventional picture of a clean Li-SEI interface that has dominated discourse in literature so far.<sup>21,29</sup> The disruption of SEI by ethanol is essential to nitrogen fixation via LiMEAS and could occur in a number of ways:

- A) **Physical attack on the SEI:** ethanol penetrates the SEI to react with lithium, forming hydrogen bubbles that damage the mechanical stability of the SEI.
- B) **Favorable SEI-forming reactions:** ethanol reacts with lithium to form an SEI that is poorly-passivating and permeable to dinitrogen.
- C) **Chemical attack on the SEI:** ethanol reacts with SEI materials, generating a more permeable interphase.

To determine which of these could be operative in our system, we employed XPS to study SEI chemistry with and without proton donor. Here we focus on the nitrogen-containing model systems (systems B and D), though spectra for all systems are included in Supplementary Fig. 23-24. Elemental analysis shows that with the addition of proton donor, the oxygen to carbon ratio in surface species increases while the fluorine to oxygen ratio decreases, implying

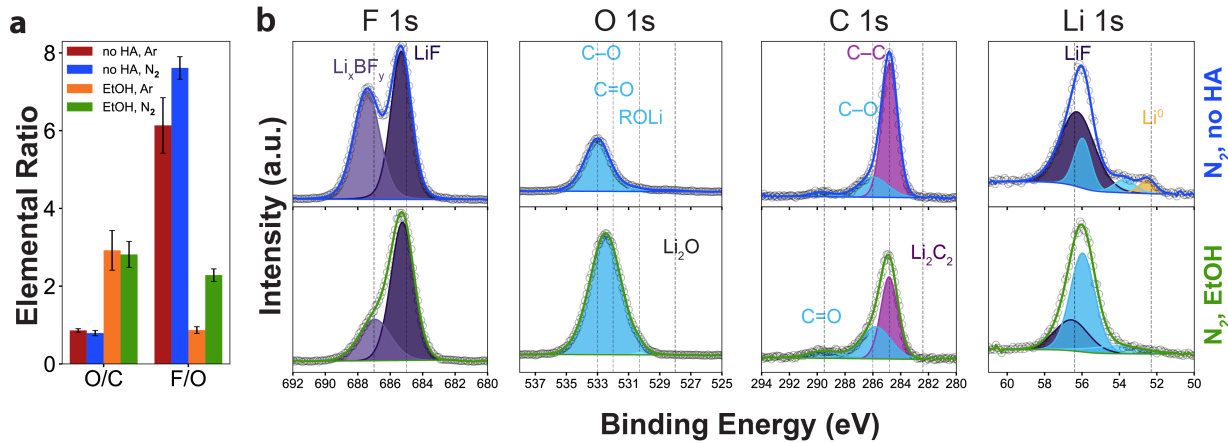
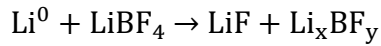


**Fig. 4 | XPS results from the four model systems.** **a**, Key elemental ratios observed in survey spectra of each system. **b**, High resolution spectra for N<sub>2</sub>, no HA and N<sub>2</sub>, EtOH systems. The intensity scale on the y-axis is consistent for plots of the same element. More spectra can be found in Supplementary Fig. 19-20.

that ethanol (a source of oxygen) may outcompete BF<sub>4</sub><sup>-</sup> (the source of fluorine) in SEI forming reactions (Fig. 4a).

High-resolution spectra reveal this phenomenon in further detail (Fig. 4b-e). In the sample without ethanol, the prominent C 1s C-C (284.8 eV) and C-O (286 eV) signals and the O 1s C-O (533 eV) peak reveal organic SEI components consistent with THF decomposition products previously documented in literature, such as alkoxides (primarily lithium butoxide) and polymeric materials (such as PTMEG).<sup>37-39</sup> With the addition of ethanol, the C 1s C-C peak decreases and the C-O signal grows, indicating organic species with shorter carbon chains, likely derived from ethanol rather than THF. The O 1s C-O signal intensity increases in samples with ethanol, widening to encompass binding energies typically associated with C=O (532 eV) and ROLi (530.3 eV) functionalities.<sup>40</sup>

In the F 1s spectra, both samples with and without ethanol show signals from LiF at 685 eV and a peak that can be attributed to other Li<sub>x</sub>BF<sub>y</sub> species at higher binding energies that originate from the reduction of LiBF<sub>4</sub> on lithium.<sup>41</sup>

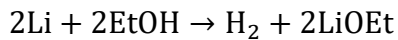


The intensities of the F 1s peaks decrease with the addition of ethanol, demonstrating a decrease in anion decomposition.

### **Proton donor as a driver of surface reactivity**

From these data, it appears that proton donor is the driver of surface phenomena in LiMEAS. In the absence of proton donor, the SEI is passivating, comprised of the breakdown products of  $\text{BF}_4^-$  and THF. Nitrogen and electrolyte cannot permeate the SEI to react with lithium, but lithium ions can diffuse through, leading to accumulation of dendritic lithium (Fig. 5a). However, with the introduction of ethanol, the SEI composition is dominated by ethanol breakdown products. Electrolyte and nitrogen can permeate this interphase, continuously consuming lithium as it deposits.

It is likely that a combination of the pathways identified above contribute to activation of the lithium surface for reaction with nitrogen. From product quantification, it is clear that ethanol reacts to form hydrogen gas, and gas generation has been shown to be associated with porous SEIs with poor mechanical stability (Fig. 5b).<sup>42,43</sup> Additionally, the generation of hydrogen gas from the reaction of lithium with ethanol coproduces lithium ethoxide:



Prior works propose that lithium ethoxide could dissolve back into the electrolyte to serve as a shuttle for protons,<sup>14</sup> but from XPS results, it is clear that some amount of ethoxide remains in solid form at the working electrode surface, participating in SEI formation. This ethoxide-rich SEI could itself be more “permeable” to nitrogen. A cryo-EM study of vitrified interfaces demonstrates that SEIs swell in the presence of electrolyte, and that swelling increases in SEIs

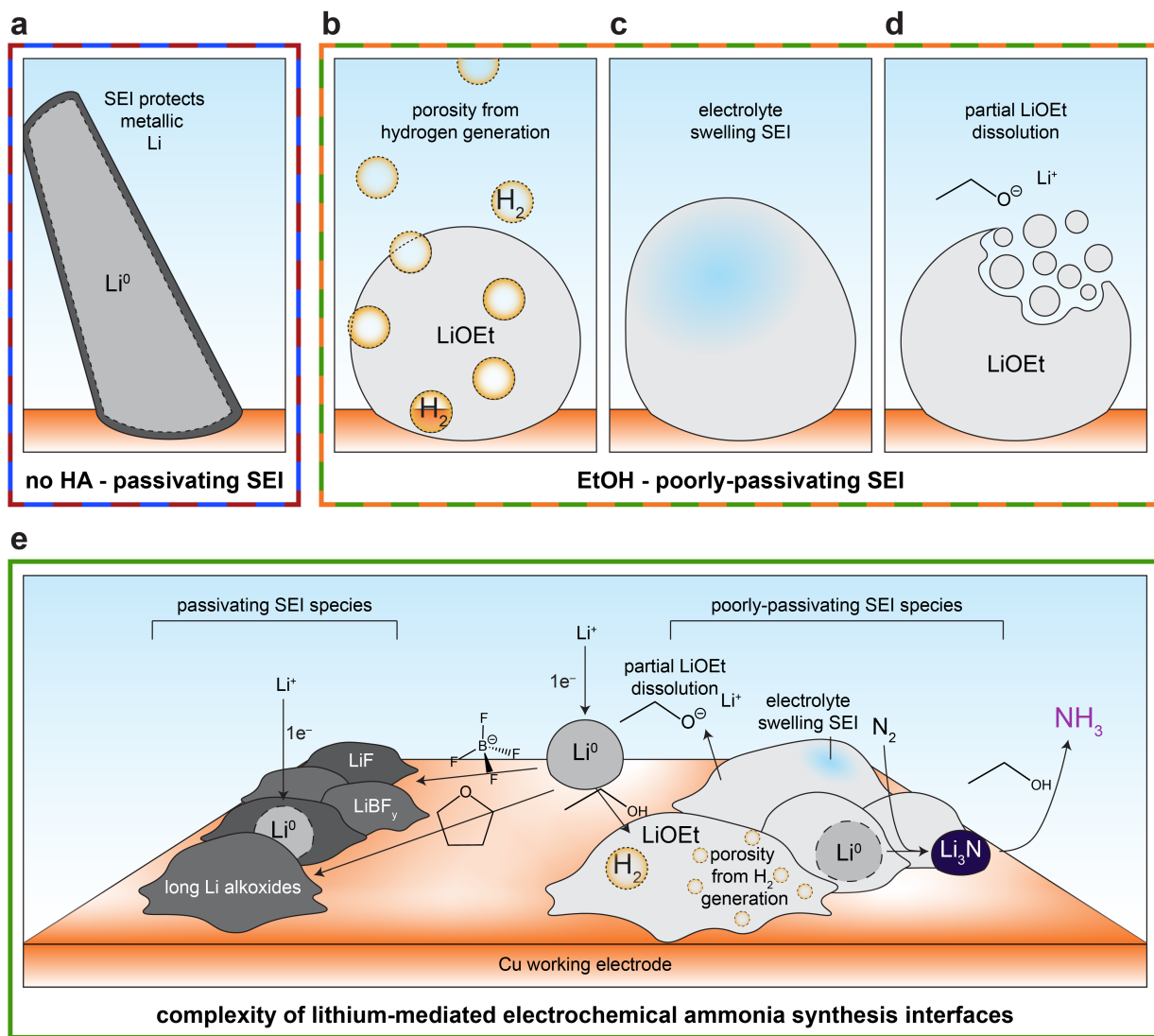


**Fig. 5 | Schematic of SEI materials and their role in LiMEAS.** **a**, Passivating SEI materials dominant in systems lacking proton donor. **b**, Poor passivation as a result of hydrogen gas generation that induces porosity in the SEI. **c**, Poor passivation as a result of a high degree of SEI swelling in electrolyte. **d**, Poor passivation because of partial solubility of SEI components, such as lithium ethoxide. **e**, Cartoon of how these phases might impact surface phenomena during LiMEAS.

with a higher proportion of organic phases, which correlates with poor electrochemical cycling (and thus poor lithium passivation).<sup>32</sup> Correspondingly, an ethanol-derived SEI may swell more in the presence of electrolyte, bringing dissolved nitrogen in closer contact with lithium and promoting continuous reactivity (Fig. 5c). Further, if lithium ethoxide is somewhat soluble in the electrolyte (Supplementary Fig. 25), the ethanol-derived SEI could lose material to dissolution (Fig. 5d).

Reactivity between ethanol or ethanol derivatives *with* the SEI is also possible. Prior work in our group has shown that even if the plating of lithium and presence of proton donor and nitrogen are separated temporally, ammonia is generated.<sup>29</sup> This implies that ethanol can attack a preexisting, electrochemically-formed SEI to facilitate lithium-nitrogen reactivity. Further discussion of possible modes of ethanol attack on the SEI can be found in the Supplementary Discussion.

### **Implications on LiMEAS mechanism**

This study indicates that the materials previously proposed to act as electrocatalysts for LiMEAS<sup>23</sup> are not abundant on the working electrode surface. Stripping experiments performed in the presence of nitrogen and ethanol detect no electrochemically-connected lithium, making it unlikely that lithium acts as an electrocatalyst. Similarly, titration measurements reveal only ~0.3% FE going toward Li<sub>3</sub>N, none of which was near enough to the surface for detection by XPS (See Supplementary Discussion). The other proposed electrocatalyst in LiMEAS is lithium hydride. Though the techniques used herein are not capable of detecting LiH, it reacts with protic molecules to form hydrogen gas<sup>44,45</sup> and is thus unlikely to be stable in the presence of ethanol. Rather, it appears that lithium and Li<sub>x</sub>N<sub>y</sub>H<sub>z</sub> species act as reactive intermediates; lithium nitridation and protonation are likely among several thermochemical pathways that consume

lithium in this process, reactions that in the battery literature would be called “chemical corrosion.”<sup>46</sup>

### Toward design principles for LiMEAS SEIs

A major implication of these findings is that functional SEIs for LiMEAS must be poorly passivating for any appreciable amount of ammonia production, the opposite of what is required for rechargeable lithium-metal batteries. This insight offers a new lens through which to interpret previous results in LiMEAS and new design principles to further tune performance. Here, we observed that SEIs rich in fluorine appear to inhibit lithium-nitrogen reactivity, and in a prior survey of proton donors for LiMEAS, we found that none of the halogenated proton donors tested were able to generate ammonia - likely because they generate halide-containing SEIs that passivate lithium.<sup>29</sup> This finding could motivate the use of non-halogenated lithium salts, which are rarely used in lithium battery research but may be particularly effective in LiMEAS for their poor passivation behavior. In this way, connecting SEI-forming reactions at the nanoscale to device-scale performance can guide the optimization of surface reactivity in LiMEAS.

### Conclusions

In this work, we took a multiscale approach combining product quantification with advanced imaging and characterization techniques to interrogate the role of surface chemistry in LiMEAS. The proton donor emerged as the key determinant of surface phenomena. In the absence of proton donor, the working electrode surface accumulates lithium in the form of dendritic deposits with a passivating SEI that prevents lithium nitridation. With proton donor, the working electrode does not retain metallic lithium, instead accumulating amorphous, nonconductive material that is dominated by ethanol breakdown products.

Together, these results reveal that lithium interfaces in LiMEAS diverge significantly from those in lithium batteries. Rather than a passivating SEI preserving the productivity of a metallic lithium deposit, the SEI in LiMEAS must allow lithium to react in a series of thermochemical reactions. This study revises our understanding of surface phenomena in LiMEAS and demonstrates that the lithium SEI can be a reactive rather than a passivating interphase.

## Methods

**Preparation of electrolyte solutions.** For experiments performed outside of the glovebox, THF (Acros Organics, ≥99%, stabilized with butylated hydroxytoluene) was dried over sieves prior to use. LiBF<sub>4</sub> (Sigma-Aldrich, ≥99%) was weighed out in an argon glovebox then transferred out of the glovebox, where dry THF was added to obtain a 1 M solution of LiBF<sub>4</sub>. The solution was centrifuged for 10 minutes at 6000 rpm to remove undissolved residue (possible contaminants), then the clear solution was transferred to oven-dried glass vials. Ethanol (VWR International, anhydrous, 200 proof, stored over sieves) was added to electrolyte requiring proton donor to make solutions of 0.1 M EtOH. Sealed electrolyte vials were stored in a desiccator and used on the day they were prepared.

For experiments performed in the glovebox, electrolyte was prepared in the glovebox. Any time solvents were used in the glovebox, the blowers of an activated carbon solvent trap (VAC Atmospheres) were turned on to increase circulation and capture excess solvent vapors. LiBF<sub>4</sub> was massed then dissolved in anhydrous THF (Sigma-Aldrich, ≥99.9%, stabilized with butylated hydroxytoluene) to make 1M LiBF<sub>4</sub> solution. The solution was capped and sealed with parafilm, then removed from the glovebox to centrifuge for 10 minutes. After centrifuging, electrolyte was returned to the glovebox without opening the centrifuge tube, then distributed into oven-dried glass vials for storage. Ethanol (purged with argon, and stored over sieves in the glovebox) was added to electrolytes requiring proton donor for a total concentration of 0.1 M. These electrolytes were also used on the day they were prepared.

**Working electrode preparation.** Copper foil (Strem Chemicals, 99.9%) was used as the working electrode in all experiments, with new foils polished on the day of each experiment. Foils were cut to approximately 15 x 15 mm squares, rinsed with deionized water, and then polished with 400 grit sandpaper followed by 1500 grit sandpaper, using more deionized water to rewet the surface and rinse the foils between sandpapers. Following polishing, foils were thoroughly rinsed with deionized water and dried in an 80°C oven for at least 20 minutes prior to use.

**Cell construction.** All experiments were performed in 2-compartment sandwich cells made of PEEK (Supplementary Fig. 1a). Copper foil was used as the working electrode, and platinum foil (Beantown chemical, 99.99%) served as the counter electrode. Cells were designed such that the exposed electrode surface area is 1 cm<sup>2</sup>. Daramic 175 was used as a separator, and aluminum foil

current collectors were placed behind the counter and working electrodes to provide points of connection for the potentiostat leads. Unused holes in cell parts were sealed with ETFE Idex plugs. All cell parts were rinsed with deionized water and dried for at least 20 minutes prior to use, and all parts except for the copper working electrodes were reused for multiple experiments. Feed gas (argon or nitrogen) was flowed at 10 sccm using an Alicat gas flow controller. The gas was bubbled through dry tetrahydrofuran to saturate the stream and minimize electrolyte evaporation before being flowed into the bottom of the cell (Supplementary Fig. 2a,b). 1.76 mL of electrolyte was added to each cell compartment prior to experiments.

**Ammonia, lithium nitride, and hydrogen quantification experiments.** Ammonia, lithium nitride, and hydrogen were measured in parallel using this procedure, which was performed outside of the glovebox. Cells were constructed as described above, taking extra care to seal the cell parts together tightly. A 16-gauge needle was used to poke a hole in the Daramic separator at the top, above the fill line of the electrolyte, to equalize pressure between cell compartments. The counter electrode compartment was sealed with a plug, and the working electrode compartment was connected to a FEP tubing outlet that led to a water bubbler (to trap excess solvent), then to the gas chromatograph (GC). To ensure that gas did not escape from the cell, the pressure drop registered by the flow controller to flow 10 sccm gas through the GC inlet was noted before experiments, then experiments proceeded only if the flow controller pressure measurement exceeded this value once the whole cell setup was constructed.

Each experiment started with 10 minutes at open circuit, then chronopotentiometry was performed at -3 mA for 20 minutes, passing 1 mAh/3.6 C in total. An 8610C SRI MultiGas 5 gas chromatograph was used for hydrogen quantification, with nitrogen as the carrier gas. Samples were injected through a 1 mL sample loop to a molecular sieve column held at 40°C. A thermal conductivity detector (TCD) was used to quantify hydrogen, and separate calibrations were performed for argon and nitrogen experiments (Supplementary Fig. 5). The GC sampling sequence lasted 5 minutes and was run on repeat throughout OCV and chronopotentiometry steps, as well as twice after the experiment ended to allow the gas from the cell time to reach the detector, a total of eight times. Hydrogen FE's were calculated by averaging the fourth through seventh hydrogen concentration points (Supplementary Fig. 4).

After the experiment, GC line was disconnected from the cell. The electrolyte was removed, with the contents of the working electrode compartment saved for ammonia quantification using the salicylate method (see below). The working electrode compartment was rinsed with ~1.76 mL of dry THF, then 1.76 mL of 0.1 M hydrochloric acid was added to protonate any residual fixed nitrogen species (e.g. lithium nitride). The acid was allowed to sit in the cell compartment for about 60 s, then removed and added to 0.5 mL of 0.4 M sodium hydroxide to neutralize. The resulting sample was quantified using the salicylate method.

**Residual metallic lithium quantification experiments.** Metallic lithium remaining on the working electrode surface after experiments was quantified using the galvanostatic stripping procedure described below, which was performed outside of the glovebox. Cells were constructed as specified above, but with a platinum wire serving as a pseudo-reference electrode (RE).

Remaining electrochemically-connected lithium on the working electrode surface was quantified using the following steps:

1. 10 min at open circuit to allow the potential to stabilize
2. 20 min chronopotentiometry, -3 mA/cm<sup>2</sup> (cathodic current, LiMEAS step)
3. 5 s at open circuit to record E<sup>Li/Li+</sup>
4. ≤ 20 min chronopotentiometry, 3 mA/cm<sup>2</sup> (anodic current, stripping step), stopping when potential reaches 0 V vs pseudo-RE
5. 1 min at open circuit
6. ≤ 20 min chronopotentiometry, -3 mA/cm<sup>2</sup> (cathodic current) to strip away lithium deposited on the platinum counter electrode during step 4.

Metallic lithium FE was calculated as follows, with the stripping time  $t_{strip}$  defined as the time needed for the slope  $\frac{dE}{dt}$  to surpass 0.03 V/s (See Supplementary Discussion):

$$FE_{Li0} = \frac{t_{strip}}{t_{LiMEAS}}$$

Taking the ratio of stripping versus deposition times is equivalent to a ratio of charge here because both steps were performed at constant currents of equal magnitude (3 mA).

**Electrochemical experiments run in glovebox.** Experiments to prepare samples for SEM, TEM, and XPS were all performed in an Ar glovebox with water and oxygen concentrations typically near 0.011 ppm and 0.1 ppm respectively. For these experiments, cells were constructed as described above, but with the separator adjusted to allow pressure equalization between the headspaces of the working and counter electrode compartments. This could be done either by using the same separators as the GC experiments, each of which had a small hole poked in the top using a 16-gauge needle, or by positioning the separators with a few millimeters of space between the top of the cell compartment and the top of the separator. The cells were stored in the oven if there was extra time between constructing them and bringing them into the glovebox.

The glovebox was plumbed with a gas line that could be used to flow argon or nitrogen saturated with electrolyte through sealed cells during experiments (Supplementary Fig. 2a). When not in use, the inlet and outlet gas lines were stored with both ends connected to each other such that they formed a loop and did not expose the glovebox to the outside environment.

Gas lines were set up such that a tee valve could select whether argon or nitrogen was flowed. While setting up the cell, regardless of the experiment, argon flowed through the gas inlet to prevent contamination of the glovebox atmosphere. Additionally, whenever the outlet gas line was not connected to a sealed cell, the valve connecting it to ventilation was shut. Upon adding electrolyte to the cell, the counter electrode compartment was sealed with an Idex plug and the working electrode compartment was connected to the outlet gas line to allow continuous flow of gas in and out of the cell without exposing the glovebox atmosphere to nitrogen or excessive solvent vapors.

All experiments started with 10 minutes of open circuit to stabilize the potential. Then, 20 minutes of -3 mA/cm<sup>2</sup> current was applied using a Tekpower TP3005T DC power supply. After current application, the gas flow was switched to argon (if not already argon), and the cell rested for about a minute while any residual nitrogen could be flushed out of the headspace to avoid contaminating the argon glovebox with nitrogen. Then, the gas outlet was disconnected, the electrolyte removed, and the cell taken apart to prepare samples for imaging or characterization.

**SEM sample preparation and imaging.** After running a constant current experiment in the glovebox as described above, the copper foil working electrode was carefully removed from the cell and gently rinsed with a few drops of anhydrous THF. Scissors were used to cut a ~1 cm long slice out of the foil, which was affixed to an SEM sample holder using conductive tape. Samples were allowed to dry in the glovebox for at least 20 minutes, then loaded into a Semilab remote-controlled air-free sample transfer shuttle. This shuttle allows for air-free transfer of samples into the SEM antechamber. All SEM imaging was conducted using a Zeiss Merlin high-resolution SEM set to an accelerating voltage of 10.00 kV with a probe current of 130 pA.

**Cryo-TEM sample preparation and imaging.** For cryo-TEM experiments, cells were constructed as described above, but with one to four TEM grids incorporated into the working electrode setup as illustrated in Fig. 3h and Supplementary Fig. 2c-e. This setup ensured that the grids were electrically connected to the copper working electrode and exposed to electrolyte, and thus could accumulate lithium and its passivation species just like the rest of the working electrode. After the experiment, the cell was deconstructed and the TEM grids were carefully rinsed with a few drops of anhydrous THF. Grids were placed on a piece of Kim wipe and allowed to dry for a few minutes, then each grid was sealed in an individual Teflon-sealed Eppendorf tube by tightly capping it and wrapping with parafilm. The Eppendorf tubes were then removed from the glovebox and quickly plunged in liquid nitrogen (LN2) to freeze. Because the pressure in the glovebox, and thus the Eppendorf tube, was greater than ambient pressure, the tubes were airtight during transfer. Bolt cutters were used to quickly break open the Eppendorf tube and expose the grid to cryogen, and tweezers were used to move the grids into a cryo-grid box for storage, all under LN2. For ease of storage and transport, polypropylene centrifuge tubes with strings attached were used to scoop up the grid boxes in LN2 and then transferred to a thermos, with the strings used to label and access individual grid boxes. Samples could be stored in the thermos under liquid nitrogen for several hours before imaging.

To conduct cryo-TEM, samples were affixed to a Gatan 626 cryo-transfer holder using a cryo-transfer station to ensure that the whole process occurred under LN2. The transfer holder's built-in shutter was kept closed over the sample while inserting the sample into the TEM column (~1s), preventing contact between the sample and air. After sample insertion, the cryo-transfer holder maintains the grid temperature at -178°C. All TEM imaging was performed using an FEI Titan 80-300 scanning transmission electron microscope (S/TEM) operated at 300kV with a field-emission gun, EDS capabilities, and ultrascan 2 × 2K digital camera (Gatan). Electron dose rate is ~10 e Å<sup>-2</sup> s<sup>-1</sup> for low magnification TEM images and ~100 e Å<sup>-2</sup> s<sup>-1</sup> for high resolution TEM images. The electron beam exposure time of each image is no more than 30s, and the acquisition time is 0.4s.

**XPS sample preparation and characterization.** After running a constant current experiment in the glovebox as described above, the cell was deconstructed. The copper foil working electrode was carefully removed from the cell and gently rinsed with a few drops of anhydrous THF. Scissors were used to cut a ~0.5 x 0.5 cm square from the Cu foil for analysis in XPS. Samples were affixed to an XPS sample holder using non-conductive tape and allowed to dry in the glovebox for at least 20 minutes. Then, the XPS sample holder was stored inside an air-free transfer vessel that enables direct transfer to the XPS sample introduction chamber without air exposure.<sup>47</sup> XPS spectra were collected using a Physical Electronics Versaprobe II X-ray Photoelectron Spectrometer.

**Ammonia quantification via salicylate assay.** The salicylate assay was used to quantify ammonia, following a procedure that has been described in prior work<sup>14,17</sup> and is elaborated on in the Supplementary Information. In brief, two solutions were prepared: 2.5 M sodium salicylate plus 0.5 mM sodium nitroprusside (“salicylate solution”) and a mixture of 10-15% NaOCl and 0.4 M NaOH in a 1:9 volume ratio (“hypochlorite solution”). Samples for ammonia and lithium nitride quantification were prepared at several different dilutions with a volume of 2 mL. To these samples, 280  $\mu$ L of salicylate solution then 280  $\mu$ L of hypochlorite solution were added in quick succession, then the samples were stored in darkness for at least 90 minutes to react, the ammonia-containing samples turning blue in color. Absorbance spectra were measured using a spectrophotometer, with the relevant quantity for calculating ammonia concentration taken to be the difference between absorbance at 650 nm and 475 nm (Supplementary Fig. 3a). The relationship between absorbance and ammonia concentration was found using calibration solutions with known amounts of NH<sub>4</sub>Cl, with a fresh calibration curve prepared each time quantification was performed (Supplementary Fig. 3b).

## References

1. FAO. *World fertilizer trends and outlook to 2022*. (2019).
2. Erisman, J. W., Sutton, M. A., Galloway, J., Klimont, Z. & Winiwarter, W. How a century of ammonia synthesis changed the world. *Nat. Geosci.* **1**, 636–639 (2008).
3. Maxwell, G. R. *Synthetic Nitrogen Products*. (Kluwer Academic Publishers, 2004).
4. MacFarlane, D. R. *et al.* A Roadmap to the Ammonia Economy. *Joule* **4**, 1–20 (2020).
5. Smith, C., Hill, A. K. & Torrente-Murciano, L. Current and future role of Haber-Bosch ammonia in a carbon-free energy landscape. *Energy Environ. Sci.* **13**, 331–344 (2020).
6. Appl, M. Ammonia , 2 . Production Processes. *Ullmann's Encyclopedia of Industrial Chemistry* 139–225 (2011) doi:10.1002/14356007.o02.
7. Chen, J. G. *et al.* Beyond fossil fuel-driven nitrogen transformations. *Science* **360**, (2018).
8. Soloveichik, G. Electrochemical synthesis of ammonia as a potential alternative to the Haber–Bosch process. *Nat. Catal.* **2**, 377–380 (2019).
9. Comer, B. M. *et al.* Prospects and Challenges for Solar Fertilizers. *Joule* **3**, 1578–1605 (2019).
10. Schiffer, Z. J. & Manthiram, K. Electrification and Decarbonization of the Chemical Industry. *Joule* **1**, 10–14 (2017).
11. Ludwig, T., Singh, A. R. & Nørskov, J. K. Subsurface Nitrogen Dissociation Kinetics in Lithium Metal from Metadynamics. *J. Phys. Chem. C* **124**, 26368–26378 (2020).
12. Tsuneto, A., Kudo, A. & Sakata, T. Efficient Electrochemical Reduction of N<sub>2</sub> to NH<sub>3</sub>

Catalyzed by Lithium. *Chem. Lett.* **22**, 851–854 (1993).

13. Tsuneto, A., Kudo, A. & Sakata, T. Lithium-mediated electrochemical reduction of high pressure N<sub>2</sub> to NH<sub>3</sub>. *J. Electroanal. Chem.* **367**, 183–188 (1994).
14. Lazouski, N., Schiffer, Z. J., Williams, K. & Manthiram, K. Understanding Continuous Lithium-Mediated Electrochemical Nitrogen Reduction. *Joule* **3**, 1–13 (2019).
15. Andersen, S. Z. *et al.* A rigorous electrochemical ammonia synthesis protocol with quantitative isotope measurements. *Nature* **570**, 504–508 (2019).
16. Greenlee, L. F., Renner, J. N. & Foster, S. L. The Use of Controls for Consistent and Accurate Measurements of Electrocatalytic Ammonia Synthesis from Dinitrogen. *ACS Catal.* **8**, 7820–7827 (2018).
17. Lazouski, N., Chung, M., Williams, K., Gala, M. L. & Manthiram, K. Non-aqueous gas diffusion electrodes for rapid ammonia synthesis from nitrogen and water-splitting-derived hydrogen. *Nat. Catal.* **3**, 463–469 (2020).
18. Suryanto, B. H. R. *et al.* Nitrogen reduction to ammonia at high efficiency and rates based on a phosphonium proton shuttle. *Science* **372**, 1187–1191 (2021).
19. Li, K. *et al.* Enhancement of lithium-mediated ammonia synthesis by addition of oxygen. *Science* **374**, 1593–1597 (2021).
20. Fichter, F., Girard, P. & Erlenmeyer, H. Elektrolytische Bindung von komprimiertem Stickstoff bei gewöhnlicher Temperatur. *Helv. Chim. Acta* **13**, 1228–1236 (1930).
21. Andersen, S. Z. *et al.* Increasing stability, efficiency, and fundamental understanding of lithium-mediated electrochemical nitrogen reduction. *Energy Environ. Sci.* **13**, 4291–4300

(2020).

22. Cai, X. *et al.* Lithium-mediated electrochemical nitrogen reduction: mechanistic insights to enhance performance. *iScience* **24**, 1–17 (2021).
23. Schwalbe, J. A. *et al.* A Combined Theory-Experiment Analysis of the Surface Species in Lithium-Mediated NH<sub>3</sub> Electrosynthesis. *ChemElectroChem* **7**, 1542–1549 (2020).
24. Peled, E. The Electrochemical Behavior of Alkali and Alkaline Earth Metals in Nonaqueous Battery Systems—The Solid Electrolyte Interphase Model. *J. Electrochem. Soc.* **126**, 2047–2051 (1979).
25. Peled, E. & Menkin, S. Review—SEI: Past, Present and Future. *J. Electrochem. Soc.* **164**, A1703–A1719 (2017).
26. Cheng, X. B. *et al.* A review of solid electrolyte interphases on lithium metal anode. *Adv. Sci.* **3**, 1500213 (2016).
27. Zachman, M. J., Tu, Z., Choudhury, S., Archer, L. A. & Kourkoutis, L. F. Cryo-STEM mapping of solid–liquid interfaces and dendrites in lithium-metal batteries. *Nature* **560**, 345–349 (2018).
28. Li, Y. *et al.* Correlating Structure and Function of Battery Interphases at Atomic Resolution Using Cryoelectron Microscopy. *Joule* **2**, 2167–2177 (2018).
29. Lazouski, N. *et al.* Proton donors induce a differential transport effect for selectivity toward ammonia in lithium-mediated nitrogen reduction. *ACS Catal.* in press (2022).
30. Cherepanov, P. V., Krebsz, M., Hodgetts, R. Y., Simonov, A. N. & MacFarlane, D. R. Understanding the Factors Determining the Faradaic Efficiency and Rate of the Lithium

Redox-Mediated N<sub>2</sub> Reduction to Ammonia. *J. Phys. Chem. C* **125**, 11402–11410 (2021).

31. Li, Y. *et al.* Atomic structure of sensitive battery materials and interfaces revealed by cryo-electron microscopy. *Science* **358**, 506–510 (2017).
32. Zhang, Z. *et al.* Capturing the swelling of solid-electrolyte interphase in lithium metal batteries. *Science* **375**, 66–70 (2022).
33. Verdouw, H., Van Echteld, J. A. & Dekkers, E. M. L. Ammonia Determination Based on Indophenol Formation with Sodium Salicylate. *Water Res.* **12**, 399–402 (1977).
34. Adams, B. D. *et al.* Accurate Determination of Coulombic Efficiency for Lithium Metal Anodes and Lithium Metal Batteries. *Adv. Energy Mater.* **8**, 1702097 (2018).
35. Xiao, J. *et al.* Understanding and applying coulombic efficiency in lithium metal batteries. *Nat. Energy* **2020** *5*, 561–568 (2020).
36. Huang, W. *et al.* Evolution of the Solid-Electrolyte Interphase on Carbonaceous Anodes Visualized by Atomic-Resolution Cryogenic Electron Microscopy. *Nano Lett.* **19**, 5140–5148 (2019).
37. Aurbach, D., Daroux, M. L., Faguy, P. W. & Yeager, E. Identification of Surface Films Formed on Lithium in Dimethoxyethane and Tetrahydrofuran Solutions. *J. Electrochem. Soc.* **135**, 1863–1871 (1988).
38. Kanamura, K., Tamura, H., Shiraishi, S. & Takehara, Z. XPS Analysis of Lithium Surfaces Following Immersion in Various Solvents Containing LiBF<sub>4</sub>. *J. Electrochem. Soc.* **142**, 340–347 (1995).
39. Zhuang, G. R., Wang, K., Chen, Y. & Ross, P. N. Study of the reactions of Li with

- tetrahydrofuran and propylene carbonate by photoemission spectroscopy. *J. Vac. Sci. Technol. A* **16**, 3041–3045 (1998).
40. Andersson, E. K. W. *et al.* Early-stage decomposition of solid polymer electrolytes in Li-metal batteries. *J. Mater. Chem. A* **9**, 22462–22471 (2021).
41. Parimalam, B. S. & Lucht, B. L. Reduction Reactions of Electrolyte Salts for Lithium Ion Batteries: LiPF<sub>6</sub>, LiBF<sub>4</sub>, LiDFOB, LiBOB, and LiTFSI. *J. Electrochem. Soc.* **165**, A251–A255 (2018).
42. Li, Y. *et al.* Revealing Nanoscale Passivation and Corrosion Mechanisms of Reactive Battery Materials in Gas Environments. *Nano Lett* **17**, 5171–5178 (2017).
43. Han, B. *et al.* Poor Stability of Li<sub>2</sub>CO<sub>3</sub> in the Solid Electrolyte Interphase of a Lithium-Metal Anode Revealed by Cryo-Electron Microscopy. *Adv. Mater.* **33**, 2100404 (2021).
44. Smith, R. L. & Miser, J. W. *Compilation of the properties of lithium hydride*. NASA Technical Memorandum (1963).
45. Aurbach, D. & Weissman, I. On the possibility of LiH formation on Li surfaces in wet electrolyte solutions. *Electrochim. commun.* **1**, 324–331 (1999).
46. Boyle, D. T. *et al.* Corrosion of lithium metal anodes during calendar ageing and its microscopic origins. *Nat. Energy* **6**, 487–494 (2021).
47. Stevie, F. A., Garcia, R., Shallenberger, J., Newman, J. G. & Donley, C. L. Sample handling, preparation and mounting for XPS and other surface analytical techniques. *J. Vac. Sci. Technol. A* **38**, 063202 (2020).

## **Acknowledgements**

This material is based upon work supported by the National Science Foundation under Grant No. 2204756. K.S. and N.L. acknowledge support from the National Science Foundation Graduate Research Fellowship under Grant No. 1745302. Data was acquired at the Electron Imaging Center for Nanomachines (EICN) at the University of California, Los Angeles's California for NanoSystems Institute (CNSI). This work also made use of the MRSEC Shared Experimental Facilities at MIT, supported by the National Science Foundation under award number DMR-1419807. We thank the staff scientists at both UCLA EICN and MIT MRSEC for their training and expertise. We also thank Matt Wolski of Daramic for providing us with polyporous separator samples, Felice Frankel for feedback on figure design, and Kindle Williams, Nathan Corbin, and all the members of the Li and Manthiram research groups for productive and helpful discussions.

## **Author contributions**

K.S., K.M, and Y.L. conceptualized the paper. K.S. developed the experimental methodology for product quantification, sample preparation for imaging and characterization, and collection of XPS spectra. X.Y. and Y.L. developed the experimental methodology for SEM and cryo-TEM. K.S. performed product quantification, SEM, and XPS experiments, and prepared samples for cryo-EM. X.Y. carried out cryo-TEM and SEM imaging. C.K. and K.S. performed the validation. K.S. wrote the original draft of the manuscript and N.L, Y.L., K.M., C.K., X.Y., and K.S. reviewed and edited its contents. K.M. and Y.L. supervised the work.

## **Competing interests**

The authors declare no competing interests.